World Scientific
www.worldscientific.com

The sparse array elements selection in sparse imaging of circular-array photoacoustic tomography

Zezheng Qin*, Yang Liu*, Junke Chi†, Yiming Ma* and Mingjian Sun*,‡

*School of Astronautics
Harbin Institute of Technology
Harbin 150000, P. R. China

†Weihai Institute of Product Quality
Standards and Metrology
Weihai 264200, P. R. China
‡sunmingjian@hit.edu.cn

Photoacoustic imaging (PAI) has been developed, and photoacoustic computed tomography (PACT) is widely used for *in vivo* tissue and mouse imaging. Simulated annealing (SA) algorithm solves optimization problems, and compressed sensing (CS) recovers sparse signals from under-sampled measurements. We aim to develop an advanced sparse imaging framework for PACT, which invloves the use of SA to find an optimal sparse array element distribution and CS to perform sparse imaging. PACT reconstructions were performed using a dummy and porcine liver phantoms. Compared to traditional sparse reconstruction algorithms, the proposed method recovers signals using few ultrasonic transducer elements, enabling high-speed, low-cost PACT for practical application.

Keywords: Photoacoustic computed tomography; sparse; simulated annealing; compressed sensing.

1. Introduction

Photoacoustic imaging (PAI) is a special existence because its signal excitation and detection combine the respective advantages of optical imaging and ultrasound imaging, thus forming a hybrid imaging technique. When the pulsed laser is irradiated to the object, the light absorber inside the object absorbs heat and locally thermally expands, thereby generating sound waves propagating outward. In practice, the source of image contrast in PAI mainly comes from optical differences.[1–7] Compared with optical imaging, PAI can provide high-resolution structural and functional imaging of deep tissues.[8–10] It has been explored for clinical research including breast, thyroid, joint and skin, internal organs of special patients, etc.[11–14]

Photoacoustic computed tomography (PACT) is one form of PAI. It can reconstruct the internal photoacoustic source distribution from ultrasound measurements in the detection plane. It can achieve

fast, high-resolution imaging at several centimeters of tissue depth.

Circular-array PACT can detect light absorbers in the circular detection area. Human applications include breast, brain, and joints. Whole body imaging is possible for small animals. The ROI is surrounded by the array, the photoacoustic waves propagating in the region of interest can be detected. Compared with the linear array and the convex array, the circular-array PACT does not have the problem of limited viewing angle and can provide high-quality images without losing boundaries.

Reliable sparse acquisition and reconstruction algorithm are crucial for restoring high-quality photoacoustic images. For the circular-array PACT system, hundreds or even thousands of array elements are required to complete the collection of photoacoustic signals according to the size of the detector and the detection aperture. Moreover, the data sampling speed is also limited by the data acquisition equipment, and the multi-channel data acquisition equipment is expensive, which will greatly increase the cost of the equipment. Traditional reconstruction methods include back-projection, filtered back-projection (FBP), and time-reversal reconstruction algorithms. These algorithms will produce a large number of artifacts in the reconstructed image when the data are incomplete, which will affect the image quality.[15–18]

In the process of sparse photoacoustic signal acquisition, domestic and foreign researchers generally use the uniform sparse sampling mode, but the premise that the photoacoustic signals collected by each array element are different is not considered. This is a compromised sparse sampling scheme, which will affect the subsequent imaging results. Bergounioux *et al.* introduce how to position sensors in thermo-acoustic tomography based on wave equation.[19] Privat *et al.* worked on the wave equation to solve the optimal array element distribution.[20] In our work, we used SA to optimize sparse element selection for different imaging target regions in sparse imaging problems based on the prior information of the imaging target.

We adopted a reconstruction strategy based on compressed sensing (CS) to replace the FBP that is usually used for a circular-array PACT. In recent years, CS has been widely studied and applied to magnetic resonance imaging (MRI), diffuse optical tomography, and computed tomography (CT). For example, Jean Provost *et al.* complete the CS

reconstruction algorithm based on circular-array PACT.[21] Michael Lustig *et al.* apply the CS to rapid MR imaging.[22] Liang Son *et al.* reported CS-based photoacoustic reconstruction in frequency domains with partially known support.[23] All these studies demonstrate that the CS-based reconstruction technique can realize the reconstruction of high-quality photoacoustic images in sparse sampling mode.

In our research, we first used SA to find the optimal sparse array elements distribution for a specific imaging target, then we can get the photoacoustic signals collected from the optimized sparse array elements.[24–28] Next, we used the sparse reconstruction algorithm based on CS to obtain a high-quality photoacoustic image. This can effectively suppress artifacts caused by under-sampling, reduce equipment costs, and increase imaging speed.

2. Method

2.1. *Photoacoustic tomography*

The generation process of the photoacoustic signal and the process of propagating ultrasonic waves can be described as follows:

$$\left(\nabla^2 - \frac{1}{c^2}\frac{\partial^2}{\partial t^2}\right)p(r,t) = -p_0(r)\frac{d\partial(t)}{dt}, \quad (1)$$

where $p(r,t)$ is the acoustic pressure signal at position r and time t, $p_0(r)$ is the initial acoustic pressure generated by pulsed laser $\partial(t)$ excitation, and c is the speed of sound. According to formula (1), the forward problem of $p_0(r)$ predicted by $p(r,t)$ can be expressed as follows:

$$p(r,t) = \frac{\partial}{\partial t}\left[\frac{1}{4\pi c^3 t}\int dr' p_0(r')\partial\left(t - \frac{|r-r'|}{c}\right)\right], \quad (2)$$

where r' refers to the position of the initial sound pressure.

2.2. *Intelligent selection of sparse array elements*

SA was first proposed by Kirkpatrick *et al.* in 1983. It is derived from the principle of solid annealing, for which a solid is heated above its recrystallization temperature for a period of time and then slowly

cooled. SA is a heuristic algorithm that has advantages in solving optimization problems. It uses Boltzmann probability distribution to jump out of the local extreme value area, thereby increasing the search for global extreme values. The initial solution and the final solution are selected randomly, which have good robustness and can better find the optimal sparse array elements distribution. First, set the initial array elements distribution, randomly select a certain array element to move in each cycle, determine whether to decide a new solution according to the change of the evaluation function, and finally find the optimal sparse array element distribution. The algorithm is based on Metropolis criterion, the probability that a particle tends to balance at temperature T is exp $(-\Delta E/T)$, where T is the temperature and ΔE is the change in internal energy. When using the simulated annealing algorithm, one starts from the initial array elements distribution X_0 and the initial value of the control parameter T, then iterates the current solution in a loop until the approximate optimal sparse array elements distribution is obtained.[29] It is a heuristic random search process guided by the Monte Carlo iterative solution method. Figure 1 shows the flow chart of the intelligent selection algorithm for the sparse elements of the circular array based on SA.

In the selection process of the sparse elements of the circular-array PACT, SA is used to find the optimal distribution of sparse elements for a specific imaging target. For each sparse array elements distribution X, the energy function $f(X)$ corresponding to X is distributed, and the minimum value of $f(X)$ is found during a gradual change of X. The energy function described in this paper is the signal-to-noise ratio (SNR) of the photoacoustic image reconstructed from the sparse photoacoustic signal. The essence of this method is an iterative process. During each iteration, when X changes, the changed X is accepted, if the energy function $f(X)$ decreases. If the energy function $f(X)$ increases, then one follows formula (3), and the Boltzmann distribution probability accepts the new X value as follows:

$$\begin{cases} \exp\left(\dfrac{f(X)_{\text{old}} - f(X)_{\text{new}}}{kT}\right), & \text{if } f(X)_{\text{new}} > f(X)_{\text{old}}, \\ 1, & \text{else} \end{cases}$$
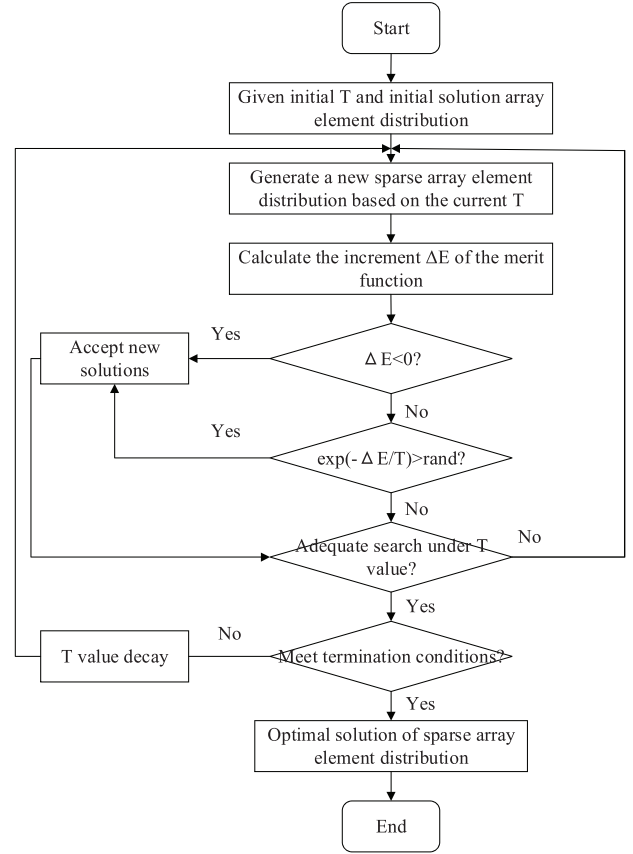$$(3)$$

Fig. 1. Flow chart of the simulated annealing algorithm.

where $f(X)_{\text{new}}$ represents the energy function value after X changes, $f(X)_{\text{old}}$ represents the energy function value before X changes, k is the Boltzmann's constant, and T is the system temperature.

2.3. Compressed sensing photoacoustic imaging

2.3.1. Compressed sensing matrix

An important application premise of CS is that the signal or its transformation in a certain transform domain is sparse or compressible. When a signal $x \in R^N$ only has elements of nonzero value ($s \ll N$), it is said to be s sparse, then the signal can be reconstructed with higher quality on the basis of much lower than the Nyquist sampling frequency. Actually, most biomedical images can be sparsed in a certain domain if we can find a suitable sparse transform. Most of the coefficient values in the transform domain are very small, and only a small proportion of large coefficients can represent most of
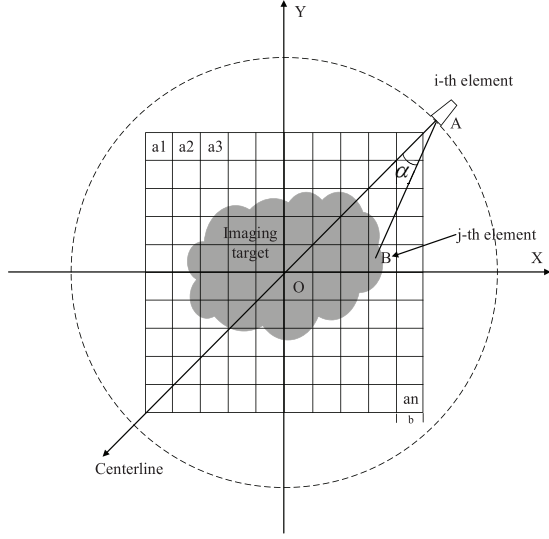
Fig. 2.   Schematic diagram of measurement matrix calculation.

the information in the image. So, in the process of photoacoustic image reconstruction, those small coefficient values can be discarded, and only a few large coefficients can be used to restore the original signal. Previous studies have shown that many sparse transformations can transform photoacoustic images into the sparse domain, including numerical derivative (ND), wavelet transform, etc. The measurement matrix K is as follows:

$$K(m,t)_{(i,j)} = \frac{1}{2\pi c}\delta\left(t - \frac{|r_{i,j} - r_m|}{c}\right),$$
$$m = 1, 2\ldots, p; \quad t = s\Delta t, \ s = 1, 2, \ldots, q_s,$$ (4)

where $r_{i,j}$ represents the coordinate value of the Cartesian coordinate system of the pixel point of the imaging area, r_m represents the position coordinate of the ultrasonic transducer, p represents the number of ultrasonic transducers, c represents the speed of sound, and q_s represents the photoacoustic, respectively. The sampling point of the signal is in the time domain. The imaging area and circular-array coordinate system of circular-array PACT are shown in Fig. 2.

The detection radius of circular-array in Fig. 2 is R, a_1–a_2 represent the N pixel grid of the imaging area, each pixel grid width is b, and the coordinates of pixel B in row i and column j are $(x_{i,j}, y_{i,j})$. The coordinate value of point A of the position of the mth ultrasonic transducer array element can be expressed as $(R\cos((m-1)\cdot\frac{2\pi}{p}) - x_{i,j}, R\sin((m-1)\cdot\frac{2\pi}{p}) - y_{i,j})$. The distance between

point A and B can be expressed as follows:

$$R_{A,B} = |AB|$$

$$= \sqrt{\begin{aligned}&\left(R\cos\left((m-1)\cdot\frac{2\pi}{p}\right) - x_{i,j}\right)^2 \\ &+ \left(R\sin\left((m-1)\cdot\frac{2\pi}{p}\right) - y_{i,j}\right)^2\end{aligned}}\cdot$$ (5)

The α in Fig. 2 represents the angle between the line segment AB and the center line of the ultrasonic transducer, which can be expressed as follows:

$$\alpha_{(i,j),m} = \arccos\left(\frac{R_{A,B}^2 + R^2 - (x_{i,j}^2 + y_{i,j}^2)}{2R_{A,B}R}\right).$$ (6)

The smaller $\alpha_{(i,j),m}$ indicates that the pixel value contributes more to the photoacoustic signal collected by the array element at that point. Therefore, the sensitivity factor is defined here to indicate the degree of contribution, and it decreases as $\alpha_{(i,j),m}$ increases, as shown in the following formula:

$$w_{(i,j),m} = \begin{cases} \cos(\alpha_{(i,j),m}), & 0 \le \alpha_{(i,j),m} \le \Omega/2 \\ 0, & \text{other} \end{cases},$$ (7)

where Ω is the receiving angle of the ultrasonic transducer.

The traditional measurement matrix is improved, and the sensitivity factor is added to make the measurement matrix more accurate. The improved measurement matrix is as follows:

$$K(m,t)_{(i,j)} = w_{(i,j),m} \cdot \frac{1}{2\pi c}\delta\left(t - \frac{|r_{i,j} - r_m|}{c}\right),$$
$$m = 1, 2\ldots, p; \ t = s\Delta t, \ s = 1, 2, \ldots, q_s.$$ (8)

Therefore, the CS equation can be written as $y = K'\theta = K'\Psi s$, and $\Theta = K'\Psi$ is called the sensor matrix. Practice has proved that for each pair of $\langle K', \Psi \rangle$, the low coherence between the two is helpful for the restoration and reconstruction of high-quality signals.

2.3.2. Compressed sensing reconstruction model

According to CS theory, the reconstruction of photoacoustic images can be obtained by solving the following constrained optimization problem:

$$\min \|\Psi\theta\|_1 \quad \text{s.t. } \|K'\theta - y\|_2 < \xi,$$ (9)

where θ is the signal to be reconstructed, K is the measurement matrix, Ψ is the sparse transformation matrix, y is the measurement value, and ξ is the maximum allowable reconstruction error. The above formula can be changed to an optimization problem of an objective function:

$$\underset{\theta}{\operatorname{argmin}} F = \|K'\theta - y\|_2^2 + \alpha\|\Psi\theta\|_1. \qquad (10)$$

A large number of experiments have proved that in the process of CS signal restoration and reconstruction, after a certain fixed sparse transformation has been adopted, the addition of total variance (TV) can further improve the quality of the reconstructed signal, so the objective function used in this paper is as follows:

$$\underset{s}{\operatorname{argmin}} F = \|\Theta s - y\|_2^2 + \alpha\|s\|_1 + \beta TV(\Psi^{-1}\theta). \qquad (11)$$

There are three parts in the objective function F. The first one is the square error between the measured value obtained by the reconstructed image through the measurement matrix and the measured value obtained by the actual system experiment. The second term represents the l_1 norm of the photoacoustic image in the sparse domain. The three items are full variation penalty items, α and β are regularization parameters to ensure the weight balance between the sparsity and consistency of the reconstructed image.

3. Results and Quantitative Analysis

First, we investigated the optimal sparse array elements selection for a specific imaging target. In the dense photoacoustic signal acquisition process of the circular-array PACT, we use a circular-array ultrasound transducer with 256 elements to collect the photoacoustic signals. In our experiments, we assumed that 256 elements were required for full sampling, and in the sparse imaging mode, we collected photoacoustic signals of 20 elements for image reconstruction. The selection of these 20 sparse array elements distribution often followed the mode of uniform sampling, that is, sampling at equal angle intervals. But, we ignored the premise that the information collected by each sensor was different. For different imaging targets, the photoacoustic signals collected by each array element are different. Choosing different sparse array elements will produce different reconstruction effects. Therefore,

we find the optimal sparse array element distribution for specific imaging targets to achieve the best imaging results. This section describes how we use SA to find the optimal sparse array elements distribution from 256 array elements to achieve the best imaging effect.

If the shape of the imaging target is circular and if the light absorption coefficient is uniformly distributed, as shown in Fig. 3(a), the photoacoustic signals collected by the ultrasonic transducers located at various angles are equally important. The uniform sparse sampling is the optimal solution at this time. But, if the imaging target shown in Fig. 3(b) is at the scanning center, the shape is not a regular circle, and the photoacoustic signal collected by the array element is different, then the uniform sparse sampling is not the optimal solution. If the imaging target locates at the position shown in Fig. 3(c), it will be difficult to achieve good imaging results with uniform sparse sampling.

We used SA to find the optimal sparse array elements distribution that achieves the best imaging effect when one or both of the following two conditions are present: (1) The imaging target is irregular and (2) the imaging target is not in the center of the imaging area. Figure 4 shows a typical imaging target. Next, we find the optimal sparse array element distribution for the target imaging based on SA.

We used SA to optimize the distribution of sparse array elements. We set the initial temperature $T = 1000$, the Markov chain length $L = 100$, the attenuation parameter $K = 0.99$, and the number of sparse array elements to 60, 40, and 20. We set the initial value PreBest X to the array element distribution of uniform sparse samplings. Our strategy for changing the position of the array elements is to randomly select an existing sparse array element each time, take each array element interval of the full array element as the unit distance, and randomly move a unit distance in the positive or negative direction. We used a cost function to calculate the SNR between the photoacoustic image reconstruction based on sparse photoacoustic signal and the photoacoustic image reconstruction based on a fully sampled photoacoustic signal. Figures 5(a) and 5(b) show the distribution of 40 and 20 optimized sparse array elements found of the imaging target shown in Fig. 4.
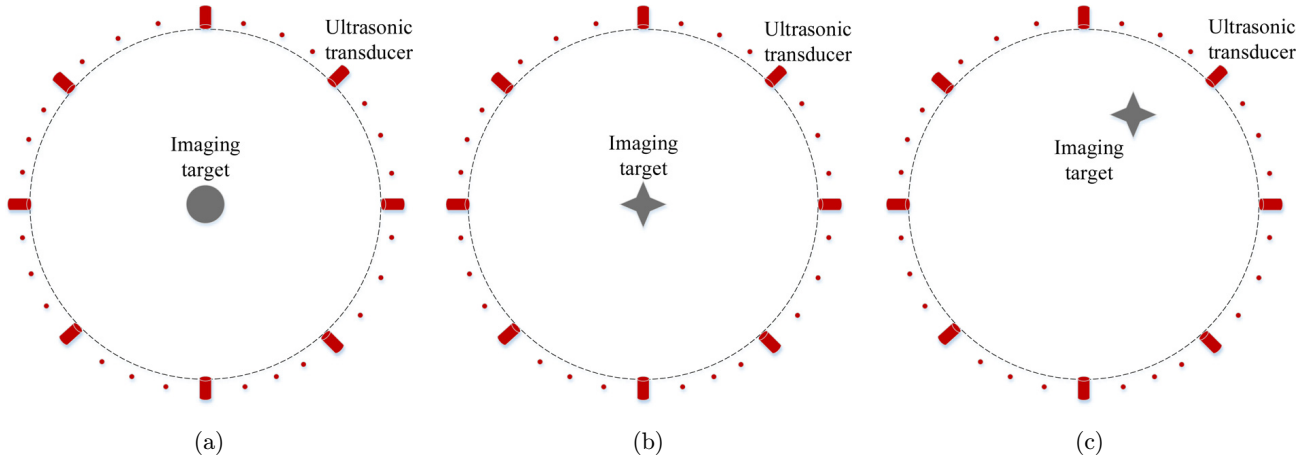
Fig. 3. Different imaging targets located in different imaging areas. (a) The circular imaging target is located in the center of the imaging area. (b) Irregular imaging target is located in the center of the imaging area. (c) Irregular imaging target is located at the edge of the imaging area.
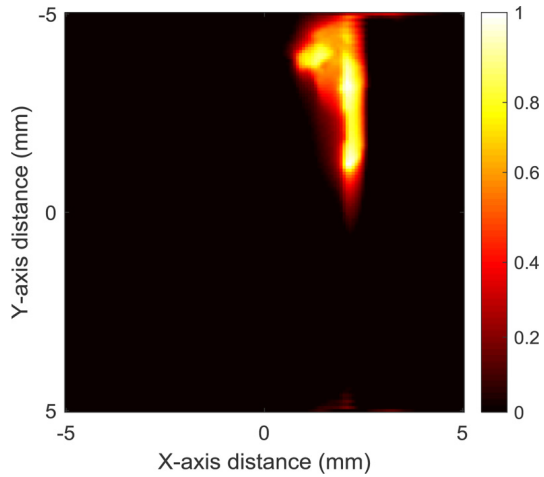

Fig. 4. A typical imaging target for a full-angle photoacoustic image reconstruction rendering.

We used the filtered back-projection (SA-FBP) and compressed sensing (SA-CS) to reconstruct the photoacoustic image based on the sparse photoacoustic signal. SA-FBP is based on FBP reconstruction, and the photoacoustic signal required for reconstruction comes from the sparse array elements selected by SA. Similarly, SA-CS can be known. We used Eq. (11) as the basic CS reconstruction model, obtained the measurement matrix using Eq. (8), and used the wavelet transform as the sparse transform base to transform the photoacoustic images.

For the imaging target of the type shown in Fig. 4, first we use SA to complete the optimal selection of sparse array elements, and then reconstruct the initial sound pressure distribution based
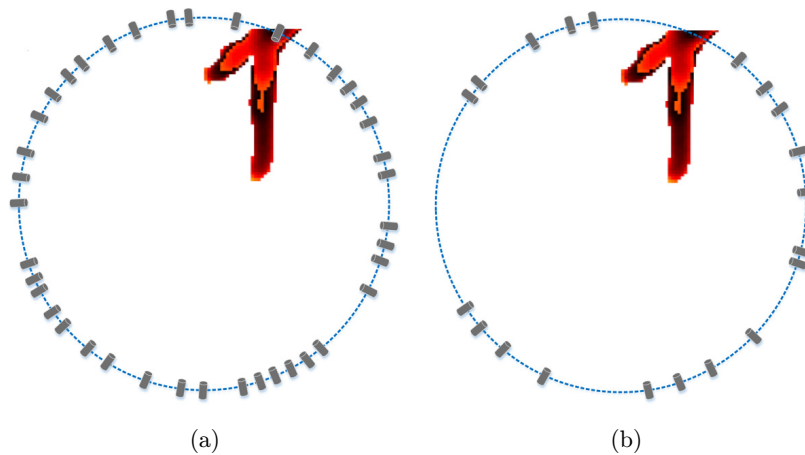

Fig. 5. Optimized sparse array elements distribution. (a) Distribution of 40 sparse array elements and (b) Distribution of 20 sparse array elements.
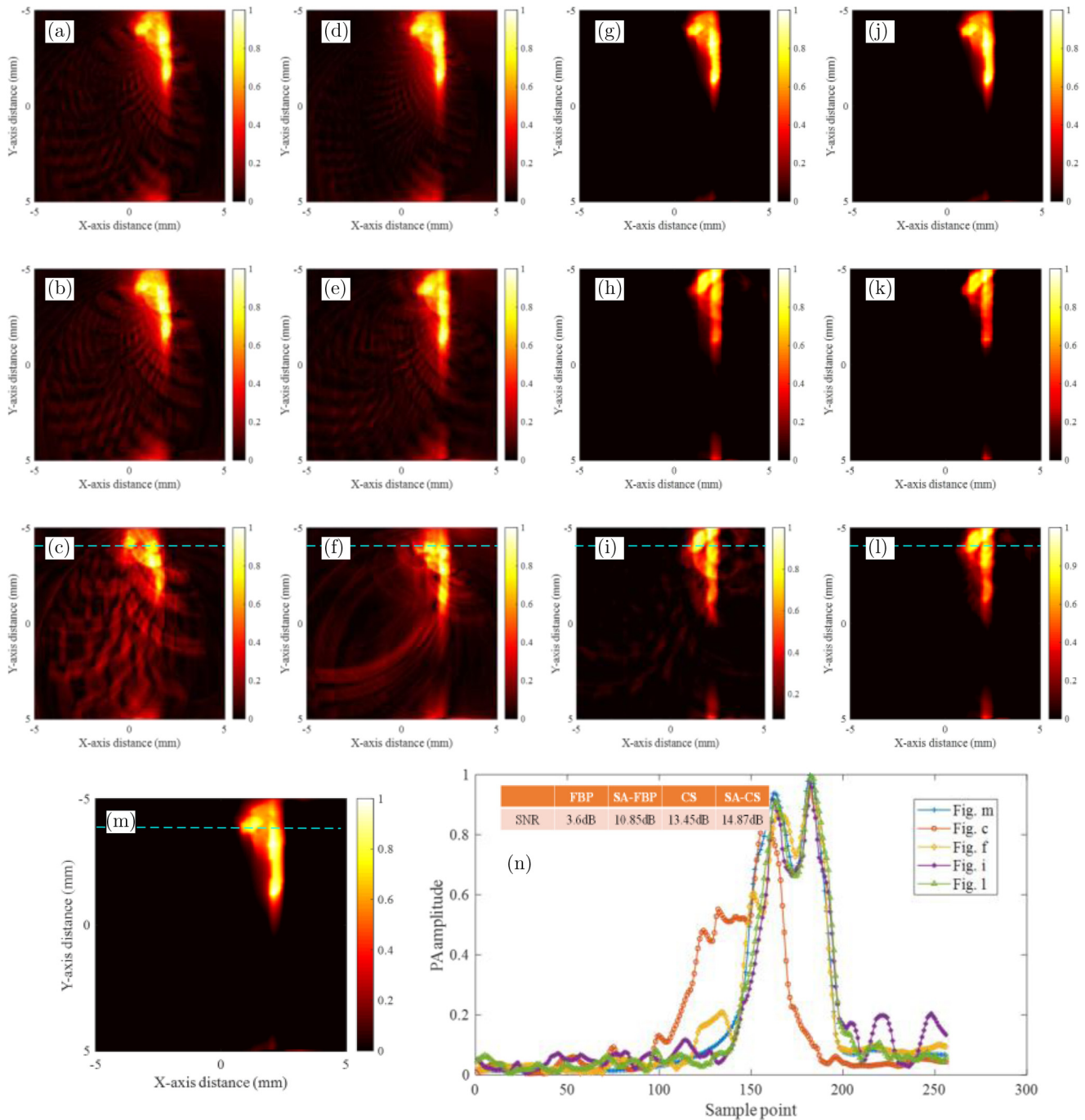
Fig. 6. PAI results. (a)–(c) PAI results reconstructed by FBP based on 60, 40, 20 array elements. (d)–(f) PAI results reconstructed by SA-FBP based on 60, 40, 20 array elements. (g)–(i) PAI results reconstructed by CS based on 60, 40, 20 array elements. (j)–(l) PAI results reconstructed by SA-CS based on 60, 40, 20 array elements. (m) PAI result reconstructed by FBP based on 256 elements. (n) The values extracted from the cyan line in picture Figs. 8(c), 8(f), 8(i), and 8(l).

on the photoacoustic signals collected by these array elements. In order to reflect the effect of the algorithm in this paper, the reconstruction results of SA-FBP and SA-CS are compared with the results of FBP and CS. Figure 6 shows that higher quality photoacoustic images can be obtained; Figs. 6(a)–6(c)

show the PAI results reconstructed by FBP based on 60, 40, and 20 array elements; the PAI results reconstructed by SA-FBP based on 60, 40, 20 array elements are shown in Figs. 6(d)–6(f), the PAI results reconstructed by CS based on 60, 40, 20 array elements are shown in Figs. 6(g)–6(i), and the

Table 1. Quantitative analysis of PAI results.

	FBP		SA-FBP		CS		SA-CS	
	SNR	SSIM	SNR	SSIM	SNR	SSIM	SNR	SSIM
20 array elements	6.75 dB	0.3895	9.43 dB	0.4456	13.36 dB	0.5832	14.48 dB	0.6125
40 array elements	13.18 dB	0.5610	14.19 dB	0.6001	17.25 dB	0.7174	17.85 dB	0.7305
60 array elements	20.56 dB	0.7713	20.67 dB	0.7938	22.12 dB	0.9024	22.16 dB	0.9103

PAI results reconstructed by SA-CS based on 60, 40, 20 array elements are shown in Figs. 6(j)–6(l). Figure 6(m) shows the PAI result reconstructed by FBP based on 256 elements, and Fig. 6(n) shows the values extracted from the cyan line in pictures for Figs. 6(c), 6(f), 6(i), and 6(l). The table in Fig. 6(n) shows the signal-to-noise ratio of the cyan-dotted pixel intensity value distribution.

In our work, the reconstructed image SNR and Structural Similarity (SSIM) were selected to evaluate the reconstruction effect. Table 1 shows that when the number of array elements used is less, the improvement of the reconstruction effect of the algorithm proposed in this paper is more obvious. This is because a smaller number of elements results in a larger variance in data acquisition. Therefore, choosing an appropriate sparse array elements distribution is particularly important in sparse reconstruction. In the FBP reconstruction algorithm, the quality of the photoacoustic image reconstructed by the optimized 20 sparse array elements is close to that of the photoacoustic image reconstructed by 40 uniformly distributed sparse array elements. Applying the optimal selection of sparse array elements to the CS reconstruction algorithm can also improve the reconstruction effect to a certain extent.

We also used the algorithm proposed in this paper to test the performance of the new imaging target shown in Figs. 7 and 8.

Figure 7 shows the optimized sparse array elements distribution based on SA for a new imaging target. The new imaging target is more complex, and this experiment verifies the universality of the algorithm in this paper. Figures 7(a) and 7(b) show the distribution of 40 and 20 optimized sparse array elements distribution, respectively. Figure 8 shows the PAI results reconstructed by FBP based on 60, 40, and 20 array elements (Figs. 8(a)–8(c)), the PAI results reconstructed by SA-FBP based on 60, 40, 20 array elements (Figs. 8(d)–8(f)), the PAI results reconstructed by CS based on 60, 40, 20 array elements (Figs. 8(g)–8(i)), and the PAI results reconstructed by SA-CS based on 60, 40, 20 array elements (Figs. 8(j)–8(l)). Figure 8(m) shows the PAI result reconstructed by FBP based on 256 elements, and Fig. 8(n) shows the values extracted from the cyan line in pictures for Figs. 8(c), 8(f), 8(i), and 8(l). The table in Fig. 8(n) shows the SNR of the cyan-dotted pixel intensity value distribution. We can find that the pixel value intensity on the cyan-dotted line of the photoacoustic image reconstructed by SA-CS is the closest to the label image.
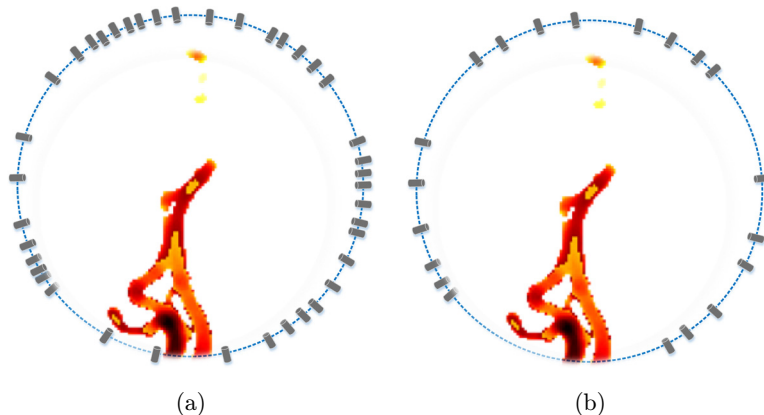

(a) (b)

Fig. 7.   Optimized sparse array element distribution. (a) Distribution of 40 sparse array elements. (b) Distribution of 20 sparse array elements.
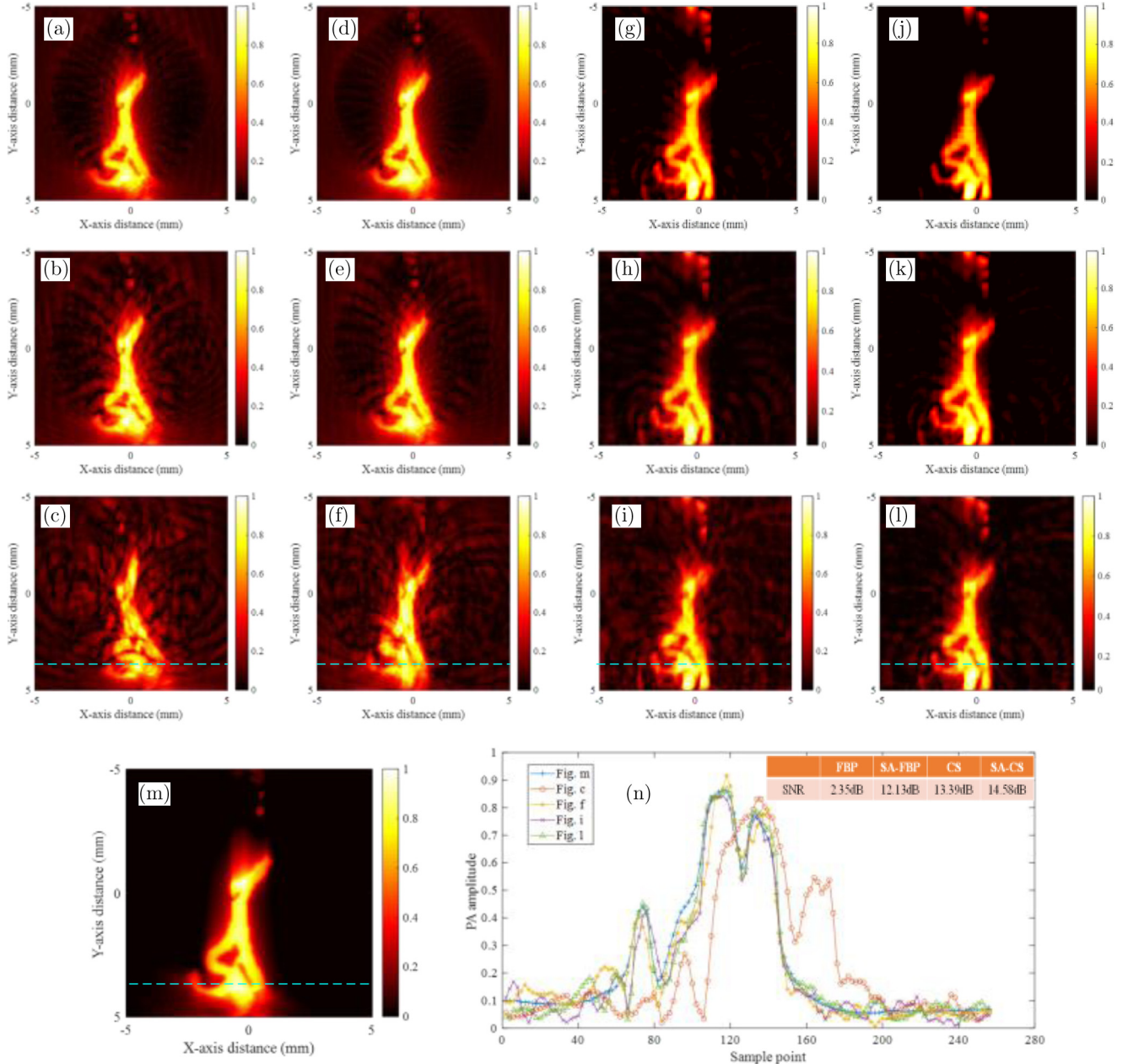
Fig. 8. PAI results. (a)–(c) PAI results reconstructed by FBP based on 60, 40, 20 array elements. (d) and (f) PAI results reconstructed by SA-FBP based on 60, 40, 20 array elements. (g)–(i) PAI results reconstructed by CS based on 60, 40, 20 array elements. (j)–(l) PAI results reconstructed by SA-CS based on 60, 40, 20 array elements. (m) PAI result reconstructed by FBP based on 256 elements. (n) The values extracted from the cyan line in picture Figs. 8(c), (f), (i), (l).

For the new imaging target, we still choose the SNR and SSIM of PAI results to evaluate the reconstruction effect, the data are shown in Table 2. Similar to the first imaging target, the algorithm in this paper also achieves a good improvement effect on complex imaging targets. It can be seen from Table 2 that the effect is particularly obvious on the imaging based on 20 sparse array elements. Using SA to optimize the selection of sparse array elements can improve the imaging quality of FBP and CS.

Figure 9 shows the PAI results based on pig liver model that we used to verify the effectiveness of the algorithm proposed in this paper. We used a 532 nm wavelength laser with a repetition rate of 20 Hz and calculated the light energy distribution on the sample to be $13.5 \, \mathrm{mJ/cm^2}$, which is below the ANSI safety limit $(20 \, \mathrm{mJ/cm^2})$. The experiment uses a

Table 2.   Quantitative analysis of PAI results.

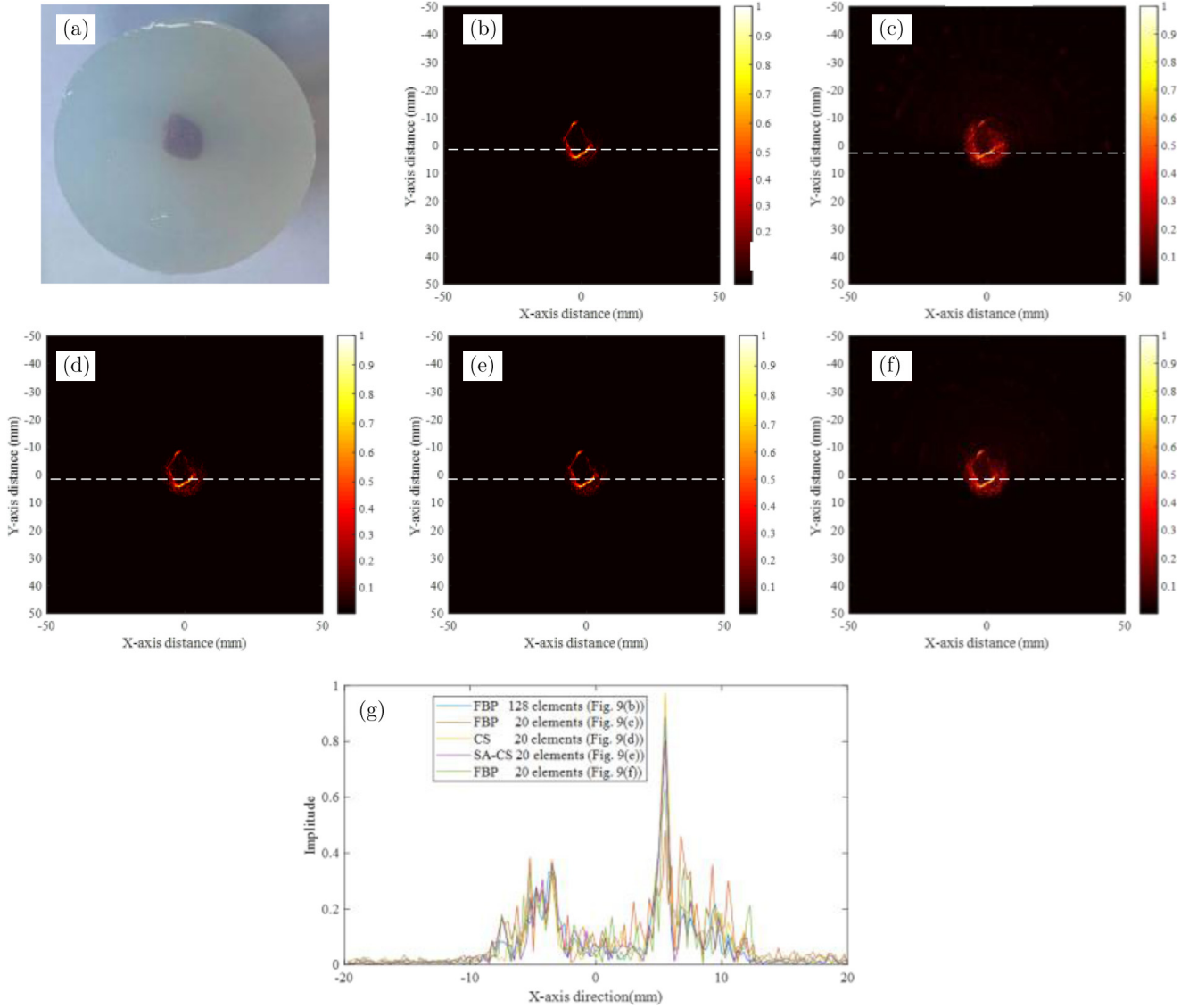|	FBP		SA-FBP		CS		SA-CS	
	SNR	SSIM	SNR	SSIM	SNR	SSIM	SNR	SSIM
20 array elements	5.75 dB	0.3572	8.39 dB	0.4321	12.57 dB	0.5975	13.29 dB	0.6123
40 array elements	11.23 dB	0.5598	12.49 dB	0.5864	16.23 dB	0.7036	17.51 dB	0.7128
60 array elements	19.83 dB	0.7532	20.01 dB	0.7863	21.58 dB	0.8745	21.65 dB	0.8887

Fig. 9.   Pig liver phantom and circular-array PAI results. (a) Pig liver phantom. (b) PAI result reconstructed by FBP based on 128 elements. (c) PAI result reconstructed by FBP based on 20 array elements. (d) PAI result reconstructed by CS based on 20 array elements. (e) PAI result reconstructed by SA-CS based on 40 array elements. (f) PAI result reconstructed by FBP based on 40 array elements. (g) The values extracted from the white line in picture Figs. 9(b)–9(f).

128-element half-circular array probe, the center frequency is 5.5 MHz, and the lighting method is annular uniform illumination. From the above experiments, it can be found that the algorithm in this paper is more suitable for application scenarios with large sparsity. Therefore, for the imaging of isolated pig liver, compared with 40 and 60, we chose to use 20 sparse array elements for imaging.

Table 3. Quantitative information of porcine liver phantom PAI results.

	MSE	SSIM	SNR
FBP result using 20-elements	0.00417	0.4567	2.5312 dB
CS result using 20-elements	0.00104	0.7527	7.4863 dB
SA-CS result using 20-elements	0.00094	0.7752	7.7061 dB
FBP result using 40-elements	0.00188	0.6354	4.6985 dB

The pig liver was put into the agar phantom to make the pig liver phantom shown in Fig. 9(a). The PAI results shown in Fig. 9 prove that the algorithm proposed in this paper has obvious effect on the imaging of isolated tissue. Figure 9(b) shows the label image. Figure 9(c) shows the PAI result reconstructed by FBP based on 20 sparse array elements, Fig. 9(d) shows the PAI result reconstructed by SA-CS based on 20 sparse array elements, Fig. 9(e) shows the PAI result reconstructed by FBP based on 40 sparse array elements. Figure 9(f) shows the pixel value intensity distribution of the white dotted line in Figs. 9(b)–9(e) to reflect the detail recovery effect. We can find that the photoacoustic image reconstructed by SA-CS based on the sparse photoacoustic signals can better display the image details. Table 3 presents quantitative information of the PAI results. We use mean squared error (MSE), SNR, and SSIM for quantitative evaluation. It can be seen from Table 3 that the images reconstructed based on SA-CS have a great improvement in both MSE and SNR. Based on the algorithm in this paper, the PAI result with 20 elements is better than the PAI result with 40 elements based on the FBP.

4. Conclusion and Discussion

It can be seen from the above experimental results that using SA to find the optimal sparse array element distribution can effectively improve the imaging effect of FBP and CS. The improvement is especially significant for FBP reconstruction algorithm, which greatly reduces the artifacts caused by incomplete data. At the same time, the sparse array elements selection based on SA can be adapted to most imaging algorithms and can be integrated into other imaging algorithms as an auxiliary imaging module. At this stage, the selection of optimized sparse array elements based on SA is mainly for specific imaging targets that require more prior information and lack flexibly. For real-time imaging, our next step is to divide the imaging area into multiple small sub-imaging areas and use SA to obtain the optimal sparse array elements distribution for imaging in each small imaging area. We will obtain the optimal sparse array element distribution corresponding to each sub-region within the imaging range to form a complete sample library. In practical experiments, the appropriate sparse array element distribution can be directly selected according to the area where the imaging target is located. It also can be applied to 3D imaging, take a small part of slices for full sampling imaging and obtain the corresponding optimal sparse array element distribution, and then guide the sparse array elements distribution of other slices for sparse imaging.

Conflicts of Interest

The authors declare no conflicts of interest.

Acknowledgments

References

1. D. Attwell, S. B. Laughlin, "An energy budget for signaling in the grey matter of the brain," *J. Cerebral Blood Flow Metabol.* **21**(10), 1133–1145 (2001).

2. D. Das, A. Sharma, P. Rajendran, M. Pramanik, "Another decade of photoacoustic imaging," *Phys. Med. Biol.* **66**(5), 05TR01 (2021).

3. L. V. Wang, S. Hu, "Photoacoustic tomography: *In vivo* imaging from organelles to organs," *Science* **335**(6075), 1458–1462 (2012).

4. E. Storkebaum, A. Quaegebeur, M. Vikkula, "Carmeliet. Cerebrovascular disorders: Molecular insights and therapeutic opportunities," *Nat. Neurosci.* **14**(11), 1390–1397 (2011).

5. N. Awasthi, S. K. Kalva, M. Pramanik, P. K. Yalavarthy, "Dimensionality reduced plug and play priors for improving photoacoustic tomographic imaging with limited noisy data," *Biomed. Opt. Exp.* **12**(3), 1320–1338 (2021).

6. W. Qiao, Z. Chen, "All-optically integrated photo-acoustic and optical coherence tomography: A review," *J. Innov. Opt. Health Sci.* **10**(4), 1730006 (2017).

7. J. Gamelin, A. Maurudis, A. Aguirre, F. Huang, P. Guo, L. V. Wang, "A real-time photoacoustic tomography system for small animals," *Opt. Exp.* **17**(13), 10489–10498 (2009).

8. Q. Shang, M. Wu, J. Yang, T. Pan, G. Zhang, D. Wu, H. Jiang, "A comparative study on water and dry coupling in photoacoustic tomography of the finger joints," *J. Innov. Opt. Health Sci.* **13**(4), 2050008 (2020).

9. L. V. Wang, Photoacoustic tomography: Omniscale imaging from organelles to patients, *Int. Conf. Photonics and Imaging in Biology and Medicine*, Optical Society of America (2017): T5A.1.

10. J. W. Ni, K. Matsumoto, H. B. Li, Y. Murakami, H. Watanabe, "Neuronal damage and decrease of central acetylcholine level following permanent occlusion of bilateral common carotid arteries in rat," *Brain Res.* **673**(2), 290–296 (1995).

11. J. T. Ye, X. Huang, Z. P. Li, F. H. Xu, "Compressed sensing for active non-line-of-sight imaging," *Opt. Exp.* **29**(2), 1749–1763 (2021).

12. L. Lin, P. Hu, X. Tong, S. Na, R. Cao, X. Yuan, "High-speed three-dimensional photoacoustic computed tomography for preclinical research and clinical translation," *Nat. Commun.* **12**(1), 1–10 (2021).

13. X. Yang, L. Xiang, "Photoacoustic imaging of prostate cancer," *J. Innov. Opt. Health Sci.* **10**(4), 1730008 (2017).

14. R. Islam, M. S. Islam, M. S. Uddin, "Compressed sensing in parallel MRI: A review," *Inte. J. Image Graph.* 2250038 (2021).

15. N. Bi, J. Tan, "Characterization of $\ell 1$ minimizer in one-bit compressed sensing," *Anal. Appl.* **17**(6), 1005–1021 (2019).

16. B. Park, C. H. Bang, C. Lee, J. H. Han, "3D wide-field multispectral photoacoustic imaging of human melanomas *in vivo*: A pilot study," *J. Eur. Acad. Dermatol. Venereol.* **35**(3), 669–676 (2021).

17. H. Lan, J. Zhang, C. Yang, F. Gao, "Compressed sensing for photoacoustic computed tomography based on an untrained neural network with a shape prior," *Biomed. Opt. Exp.* **12**(12), 7835–7848 (2021).

18. Z. Guo, C. Li, L. Song *et al.*, "Compressed sensing in photoacoustic tomography *in vivo*," *J. Biomed. Opt.* **15**(2), 021311 (2010).

19. M. Bergounioux, E. Bretin, Y. Privat, "How to position sensors in thermo-acoustic tomography," *Inverse Probl.* **35**(7), 074003 (2019).

20. Y. Privat, E. Trélat, E. Zuazua, "Optimal observation of the one-dimensional wave equation," *J. Fourier Anal. Appl.* **19**, 514–544 (2013).

21. J. Provost, F. Lesage, "The application of compressed sensing for photo-acoustic tomography," *IEEE Trans. Med. Imaging* **28**(4), 585–594 (2008).

22. M. Lustig, D. Donoho, J. M. Pauly, "Sparse MRI: The application of compressed sensing for rapid MR imaging," *Magn. Reson. Med.* **58**(6), 1182–1195 (2007).

23. J. Meng, L. V. Wang, L. Ying *et al.*, "Compressed-sensing photoacoustic computed tomography *in vivo* with partially known support," *Opt. Exp.* **20**(15), 16510–16523 (2012).

24. J. Frausto-Solis, J. P. Sánchez-Hernández, M. Sánchez-Pérez, "Golden ratio simulated annealing for protein folding problem," *Int. J. Comput. Meth.* **12**(6), 1550037 (2015).

25. D. Delahaye, S. Chaimatanan, M. Mongeau, Simulated annealing: From basics to applications, *Handbook of Metaheuristics*, International Series in Operations Research & Management Science, Vol. 272, pp. 1–35, Springer, Cham (2019).

26. M. A. Mohammed, D. A. Ibrahim, A. O. Salman, "Adaptive intelligent learning approach based on visual anti-spam email model for multi-natural language," *J. Intell. Syst.* **30**(1), 774–792 (2021).

27. A. Madkour, M. A. Hossain, K. P. Dahal, H. Yu, "Intelligent learning algorithms for active vibration control," *IEEE Trans. Syst. Man Cybernet. C Appl. Rev.* **37**(5), 1022–1033 (2007).

28. H. Li, X. Wan, T. Liu, Z. S. Liu, Y. H. Zhu, "A computed tomography reconstruction algorithm based on multipurpose optimal criterion and simulated annealing theory," *Chin. Opt. Lett.* **5**(6), 340–343 (2007).

29. R. A. Rutenbar, Simulated annealing algorithms: An overview. *IEEE Circuits and Devices Magazine* **5**(1), 19–26 (1989).